Plasma Sources Science and Technology

PAPER • **OPEN ACCESS**

Continuous gas temperature measurement of cold plasma jets containing microdroplets, using a focussed spot IR sensor

To cite this article: N Hendawy *et al* 2020 *Plasma Sources Sci. Technol.* **29** 085010

OPEN ACCESS
IOP Publishing
Plasma Sources Science and Technology
Plasma Sources Sci. Technol. **29** (2020) 085010 (9pp)
https://doi.org/10.1088/1361-6595/aba2aa

Continuous gas temperature measurement of cold plasma jets containing microdroplets, using a focussed spot IR sensor

N Hendawy[1], **H McQuaid, D Mariotti and P Maguire**

NIBEC, Ulster University, Belfast, BT37 0QB, United Kingdom

E-mail: Hendawy-n@ulster.ac.uk

Received 12 June 2020
Accepted for publication 3 July 2020
Published 13 August 2020

Abstract

Controlling gas temperature via continuous monitoring is essential in various plasma applications especially for biomedical treatments and nanomaterial synthesis but traditional techniques have limitations due to low accuracy, high cost or experimental complexity. We demonstrate continuous high-accuracy gas temperature measurements of low-temperature atmospheric pressure plasma jets using a small focal spot infrared sensor directed at the outer quartz wall of the plasma. The impact of heat transfer across the capillary tube was determined using calibration measurements of the inner wall temperature. Measured gas temperatures varied from 25 °C–50 °C, increasing with absorbed power and decreased gas flow. The introduction into the plasma of a stream ($\sim 10^5$ s^{-1}) of microdroplets, in the size range 12 μm–15 μm, led to a reduction in gas temperature of up to 10 °C, for the same absorbed power. This is an important parameter in determining droplet evaporation and its impact on plasma chemistry.

Keywords: IR sensor, gas temperature, atmospheric pressure plasma, microdroplets, aerosol

(Some figures may appear in colour only in the online journal)

1. Introduction

Continuous and reliable measurement of gas temperature in atmospheric pressure plasmas (APP) is critical for future applications in plasma medicine, food and agriculture as well as nanomaterials synthesis. APP systems cover a wide variety of configurations, geometries and temperature ranges. In non-thermal equilibrium APPs there is generally a desire to maintain temperatures as low as possible. However, there is also an understanding that gas temperature can be sensitive to many factors that are rarely well-characterised or controlled, especially with the inclusion of molecular gases and water as environmental feedback factors. Gas temperature increase in APPs is due to the high electron and particle collisionality of these systems [1]. Most chemical and combustion reactions are strongly dependent on gas temperature [2], as are surface reactions and neutral radical distributions and their kinetics [3, 4]. Additionally in many biomedical and material applications a controlled heat load is required for the treatment of heat sensitive surfaces e.g. wound tissue and polymers [5]. Issues such as feedback process control, process stability/repeatability, regulatory, or end-user approval, require a capability for inline monitoring of temperature and rapid response to fluctuations or thermal runaway.

The various techniques to measure gas temperature include optical emission spectroscopy (OES) [1, 6–15], infrared thermometry [1, 16–18], millimetre wave interferometry [19],

[1] Author to whom any correspondence should be addressed.

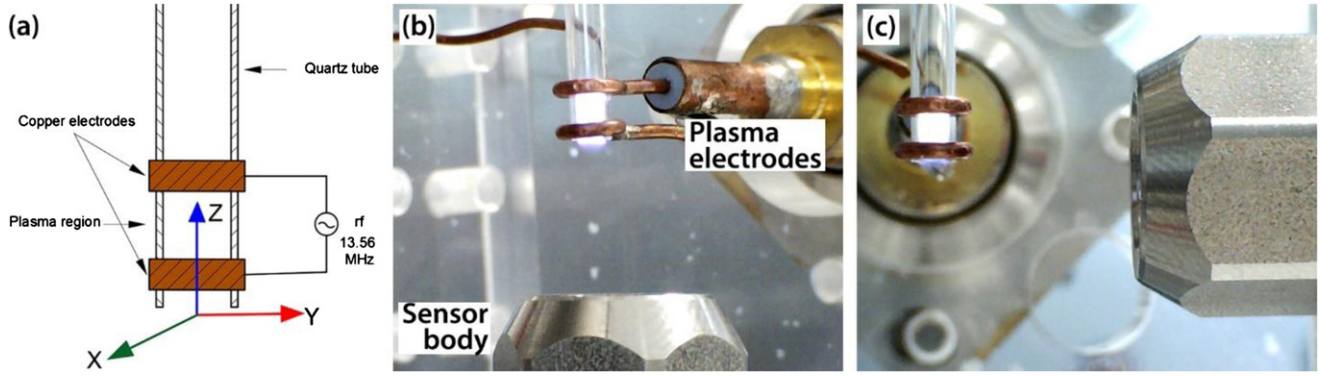

Figure 1. (a) Schematic of the plasma setup with axis labels, (b) vertical orientation for inner wall temperature measurement and (c) horizontal orientation for outer wall measurement.

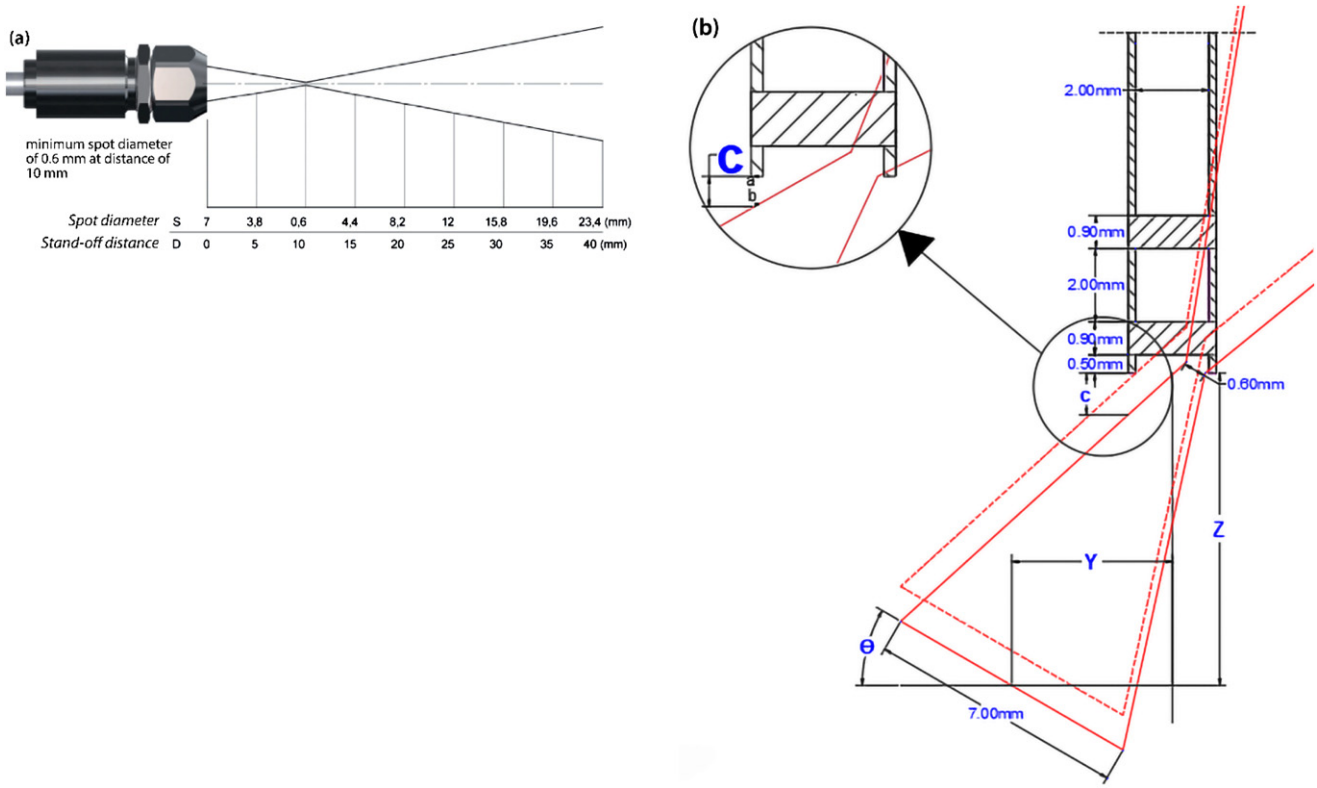

Figure 2. (a) IR sensor optic field profile showing spot diameter versus stand-off distance and (b) CAD drawing of the geometric setup of the plasma capillary and IR probe, in vertical configuration for inner wall measurement. Overlay shows the positions of the optic field profile outlines, initially (red, dashed) and after translation in the *Z*-axis (red, solid), where the initial clearance between upper edge of the optic field and quartz wall is 0 mm and the final clearance is *c* mm.

Schlieren [1, 5], Rayleigh scattering [20, 21], thermocouple [1, 11, 22, 23], and fibre optic based thermometry [24, 25]. These have been applied to a varying degree in different plasma systems including plasma torch [15, 26, 27], dielectric barrier discharge [1, 7, 14, 18, 19], plasma jet [5, 8, 9, 16, 20, 24, 27, 28], gliding arc discharge, [2, 17, 25] and glow discharge [21]. While some methods offer high accuracy, they are not suitable for continuous measurement due to size and cost and have generally been used to provide a calibrated reference for other techniques, particularly OES, which is a routine and non-invasive technique. OES obtains a gas temperature estimate by fitting the experimental spectra to theoretical spectra of chosen molecular species, for example N_2, NO, OH or CN [20, 27]. However the population of the rotational energy levels, derived from the observed emission cannot automatically be assumed to be in equilibrium with the translational states i.e. gas temperature [2, 28]. Iseni *et al* [29] compared the analysis of broadening (line, resonance and Van der Waals) of specific isolated lines with the analysis of the rotational distribution of diatomic molecules as methods to determine neutral gas temperatures. They provide estimates of uncertainties of 3%–6% and 4%, respectively. Since high resolution spectrometer instrumentation is not viable for continuous sensing, the inability to resolve the rotational structures leads to a fitting process which can be complex, slow, difficult to automate, and with accuracy levels strongly dependent on

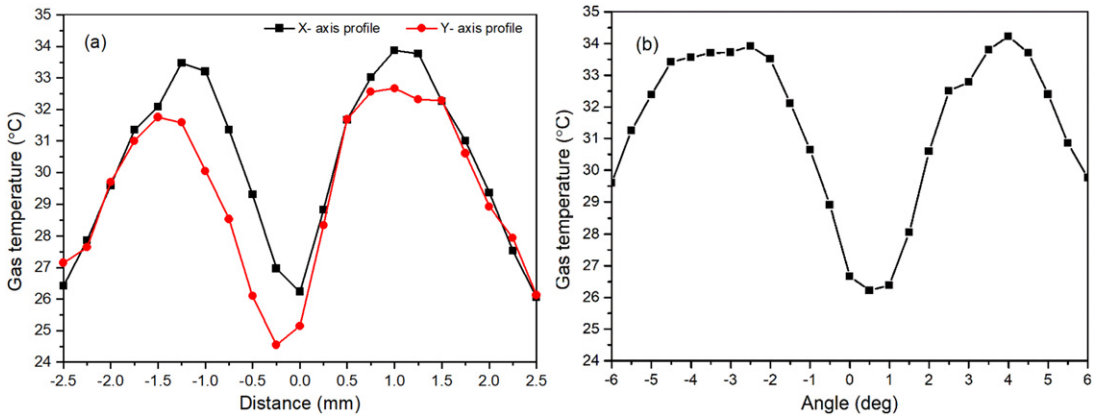

Figure 3. Determining the alignment of sensor with respect to the quartz tube axis from temperature profiles across the tube by (a) varying *X* and *Y* distances and (b) angle of inclination.

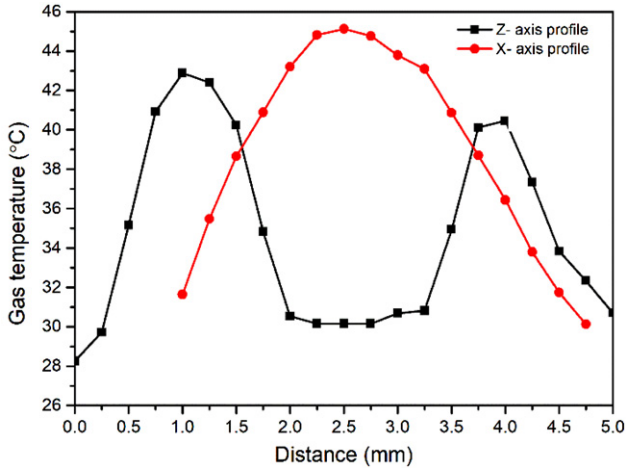

Figure 4. Vertical and horizontal temperature profile of the outer surface of the capillary with the IR probe in the horizontal position. The peaks in the *z*-axis profile indicate the Cu electrode temperature. An emissivity value of 0.93 (quartz) was used and temperature values are valid only for the quartz region. Assuming a Cu emissivity range of 0.5 to 0.8 for unpolished/rolled metal, gives a maximum upper electrode temperature in the range 50 °C–80 °C.

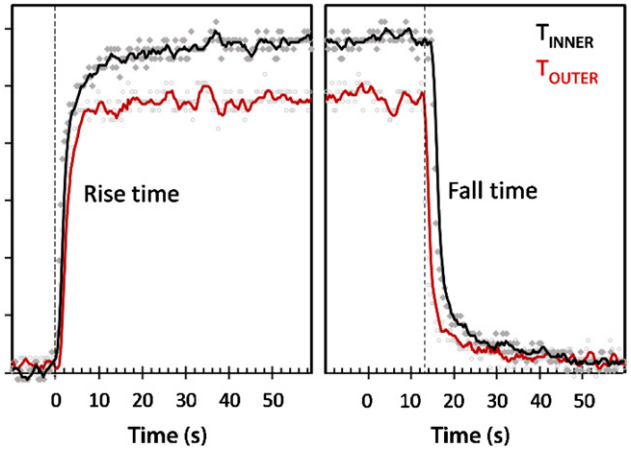

Figure 5. Temperature rise and fall times for inner wall (black) and outer wall (red). Dashed lines indicate the plasma ignition and extinction times obtained from photodiode response.

apparatus parameters [2, 27]. Temperature resolution is of the order $\geqslant$50 K in cold plasmas unless high resolution spectra are available.

Other potential inline measurement techniques such as thermocouple (TC), fibre optic (FO) thermal indicators and traditional infrared-emission (IR) are also problematic [30]. Permanently locating the TC or FO into the gas stream is often inhibited by geometric restrictions, flow disruption, contamination and electrical coupling concerns. Traditional IR measurements provide an average wall temperature value over the field of view (FoV) and at typical sensor stand-off distances, the FoV is unsuitable for many plasma systems because of size or temperature non-uniformity. Thermal imaging using cooled high resolution IR cameras can improve the spatial resolution but this technique is reserved for stand-alone experiments, often at high temperatures [31–35].

Previously we have used OES spectra of OH lines to determine the impact of APP heating on nanoparticle synthesis with an estimated fit error of $\pm$50 K, for temperatures around 600 K in dry Ar [36]. However, with added water, the use of the OH lines leads to heightened error margins due to electronic quenching of OH (A-X) emission by H_2O molecules [37]. This effect becomes noticeable at 100–300 ppm H_2O and above [38]. Microdroplet transport through plasma jets can generate beneficial enhancement and transport of radical species (e.g. $OH^{\bullet}$, H_2O_2), important electron reduction reactions and rapid nanomaterials synthesis [39, 40]. The chemical kinetics are thought to depend on droplet evaporation which in turn is sensitive to gas temperature. However the OES derived temperature estimates, obtained using OH lines, exhibit significant differences compared to using the N_2 lines, once droplets are introduced into the plasma [6]. Here we investigate the use of a small form factor IR sensor for continuous monitoring of gas temperature of an RF plasma jet contained in a narrow quartz capillary tube. The plasma region is defined by two outer ring electrodes which are separated by a distance $\geqslant$2 mm. The sensor FoV diameter is 0.6 mm at a stand-off distance of 10 mm. It is expected that the inner wall temperature of the capillary in contact with the plasma will rapidly reach equilibrium with

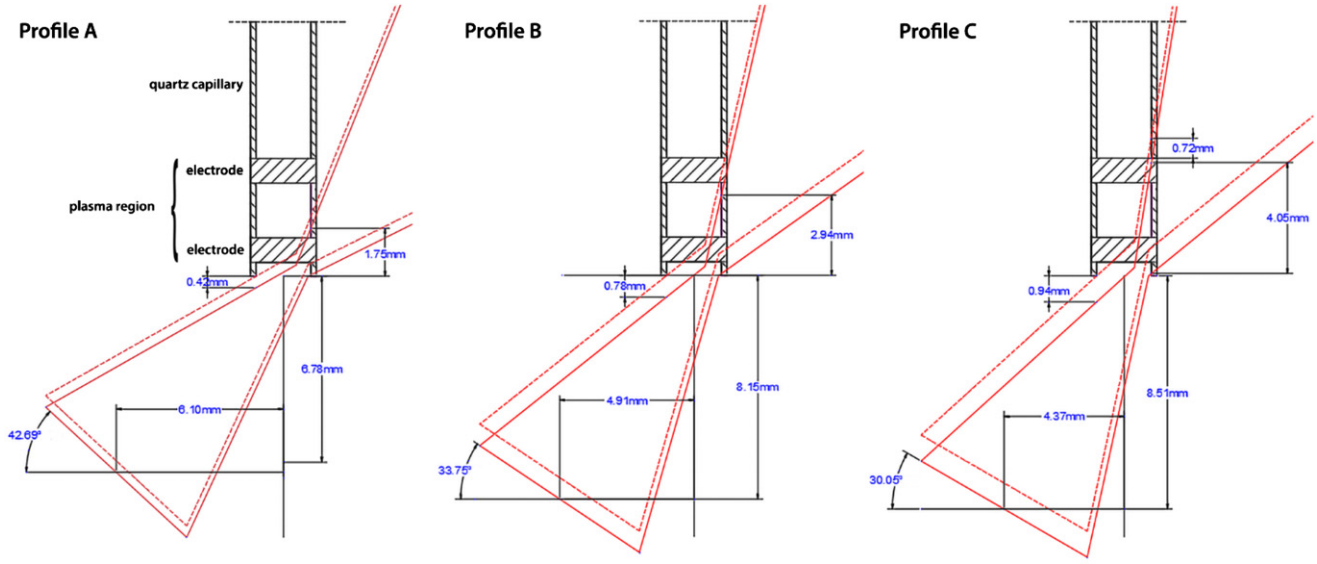

Figure 6. CAD drawings of initial IR sensor positions and inclinations showing the intersection of optical field with inner wall. The optical field profile (solid red) is obtained from manufacturers specifications (see figure 2(a)), the dashed lines indicate maximum Z-axis travel for $c > 0$.

Table 1. Values for initial IR sensor positions and inclinations according to CAD drawings in figure 6. X and Y are the distances (mm) from the capillary centreline, Z is the distance from the sensor to the capillary, c is the clearance before the optic field hits the wall, Θ is the angle of inclination with x-axis and D is the diameter of optical spot in mm.

	$Y(0)$ mm	$Z(0)$ mm	$\Theta(0)$	c(final) mm	D mm
Profile A	6.10	6.78	42.69°	0.42	1.75
Profile B	4.91	8.15	33.75°	0.78	2.94
Profile C	4.37	8.51	30.05°	0.94	4.05

the plasma gas temperature and represent a close approximation. In order to determine the temperature gradient across the quartz, i.e. between inner and outer walls, we first measure the temperature of the inner wall in contact with the plasma with the sensor placed at the capillary exit and directed along the capillary axis. Precisely locating the sensor FoV within the plasma region is achieved with reference to a known geometrical setup, by scanning the sensor in XYZ directions and over a range of angles. After obtaining calibration measurements of outer wall against inner wall temperature for varying power, flow and He/Ar gas mixture, we then determine gas temperature in the presence of microdroplets from the outer wall temperature.

2. Methods

Figure 1 shows a schematic and a photo of the experimental apparatus. The plasma is generated inside a capillary quartz tube 2.00 mm inner diameter (0.2 mm thickness). Radio frequency (RF) power at 13.56 MHz is connected to two concentric copper ring electrodes with a 2 mm separation, with the quartz tube extending 1 mm below the lower electrode. He, Ar and Ar/He gas flows from 0.5 to 3.0 slm without droplets were controlled by MKS G-Series mass flow controller. The net RF

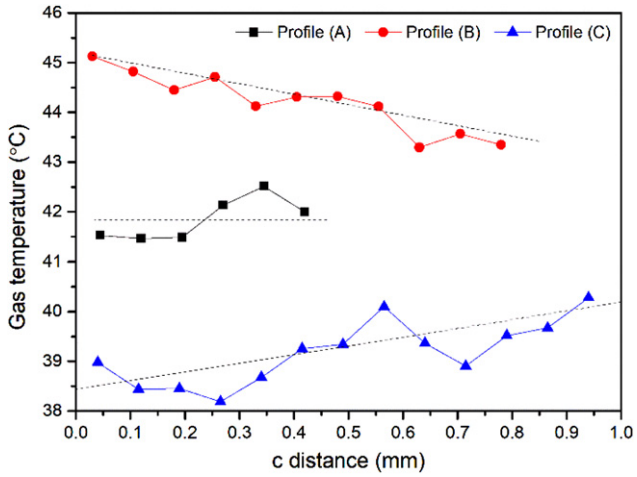

Figure 7. Temperature profile of the inner wall of the capillary tube versus clearance, c, between bottom of quartz tube and the upper edge of the optic field profile (see figure 2(b)). Note in figure 6, the minimum clearance is shown by the dashed profile and maximum by the solid.

power, as determined using an Octiv Suite 2.0 VI Probe, is varied from 0.05 W to 0.6 W. For microdroplet studies, microdroplets with average diameters in the range 12 μm–15 μm were obtained from a Burgener Mira Mist X-175 nebuliser and were injected into a helium gas flow (Q_1) of 0.7 slm upstream of the plasma. The nebuliser was driven by a separate He gas flow (Q_2) and the total plasma gas flow was $Q = Q_1 + Q_2$. The liquid (H_2O) was supplied from a syringe pump at 4 μl min^{-1} and an estimated 5 $\times$ 10^4 droplets per second were delivered into the plasma [6, 39]. Infrared temperature measurements were obtained using a Micro-Epsilon thermometer CT precise infrared sensor (CT-CF22-C1 Miniature-Pyrometer) with spectral range 8–14 μm and integrated CF lens providing a focal spot diameter of 0.6 mm at a stand-off distance of 10 mm [41].

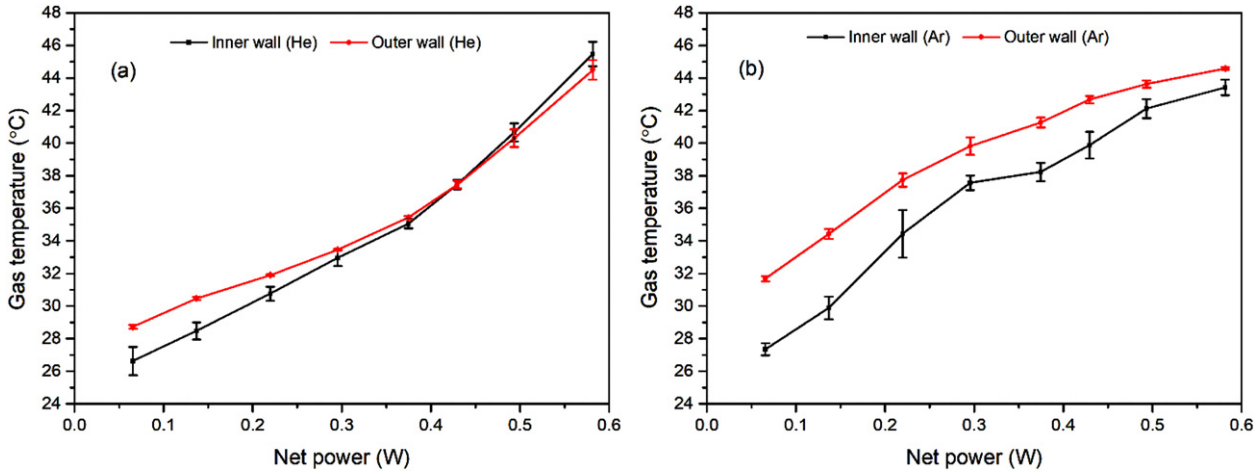

Figure 8. Inner and outer wall temperature of the capillary tube against RF net power at a fixed flow rate of 1.0 slm for (a) He and (b) Ar plasmas. Error bars represent the standard error ($n = 3$).

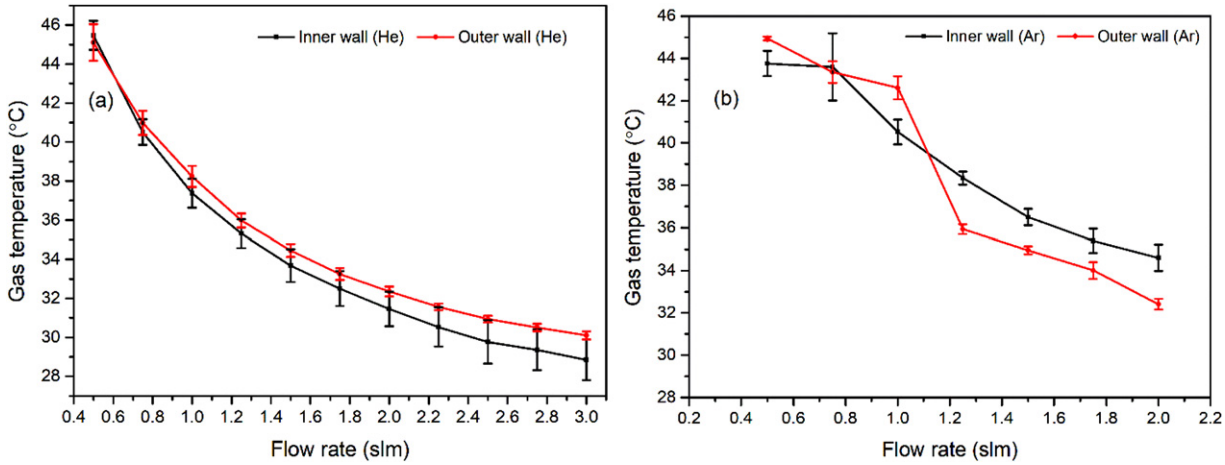

Figure 9. Inner and outer wall temperature of the capillary tube against flow rate at a fixed RF net power of 0.3 W for (a) He and (b) Ar plasmas. Error bars represent the standard error ($n = 3$).

In normal operation, the sensor face is positioned at a stand-off distance from the outer wall of the quartz tube to collect emission from between the copper electrodes, figure 1(c). In order to calibrate the temperature gradient across the thin quartz wall, calibration measurements of the inner wall temperature between the electrodes are obtained with the setup shown in figure 1(b), with the sensor pointing upwards along the capillary axis. The variation in sensor FoV with stand-off distance is given in figure 2(a) and the sensor position relative to the capillary exit, in the configuration of figure 1(b), is shown in the CAD drawing of figure 2(b), with the optic field profile overlaid (red). The 7 mm wide sensor face is inclined at angle θ with its centreline situated X mm and Y mm from the capillary axis and Z mm from the capillary exit. To obtain an optic field intersection with the inner wall, of diameter D, within the region bounded by the two electrodes, the sensor XYZ position and angle θ is varied in increments of 0.25 mm and 0.5 degrees, respectively. The clearance, c, between the upper edge of the optic field and the bottom of the quartz tube determines the limit of sensor vertical movement. Firstly, the precise centreline (axis) of the tube is determined by scanning the sensor in x- and y-directions with a nominal 0° inclination. The resultant temperature profile, figure 3(a) shows two peaks indicating the wall positions and the centreline is assumed to be at the lowest temperature between the walls. The sensor is then positioned at this centreline axis and the temperature is obtained while the inclination is varied using a precision rotation platform (5 arcmin resolution), figure 3(b). The reference 0° inclination is taken as the angle at which the minimum temperature occurs.

To locate its normal position reading the outer wall temperature at the centre of the plasma, the sensor is set at a stand-off distance of 10 mm, with an FoV diameter at the outer quartz wall of 0.6 mm, figure 1(c). The sensor is scanned in the horizontal direction (X), to determine the tube limits and central axis, and in the vertical direction to locate the two electrodes and obtain plasma temperatures in the interval. The temperature peaks in the z-axis profile of figure 4 represent the Cu electrodes. The actual value of temperature is unknown since the emissivity of Cu varies considerably (0.1 to 0.9) based on

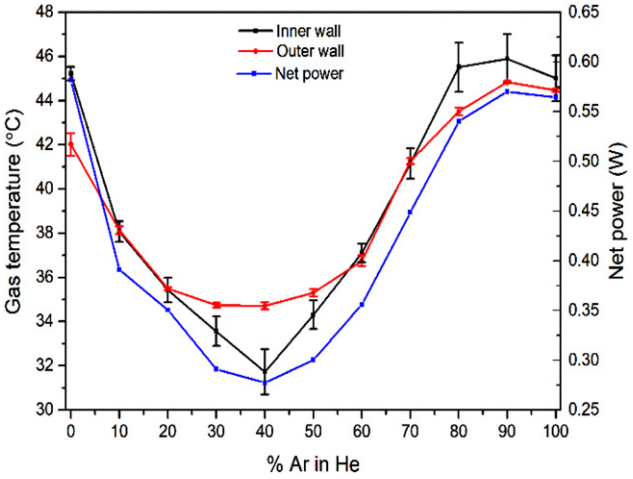

Figure 10. Inner wall temperature versus Ar:He mixture at total flow rate of 1.5 slm and maximum net power of 0.58 W. Also shown is the variation in absorbed power with Ar:He ratio. Error bars represent the standard error ($n = 3$).

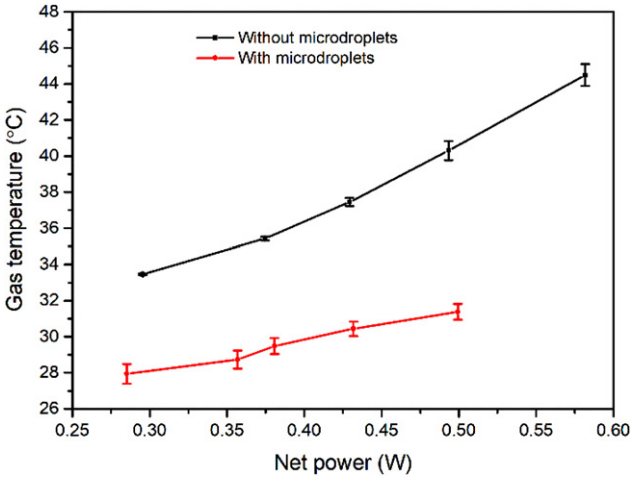

Figure 11. Gas temperature against RF net power in He without and with microdroplets at flow rates of 1.5 slm. Error bars represent the standard error ($n = 3$).

surface condition. Assuming a Cu emissivity range of 0.5 to 0.8 for unpolished/rolled metal, gives a maximum upper electrode temperature in the range 50 °C–80 °C. The distance between temperature peaks in the vertical (Z) profile, figure 4, is ∼3 mm, equivalent to the 2 mm gap between electrodes and accounting for electrode thickness and FoV diameter. The constant temperature valley extends ∼1.5 mm and this provides the average plasma temperature.

The IR sensor readings are available every 1 ms. Transient thermal response characteristics are shown in figure 5 for both inner and outer wall measurements. Plasma ignition and extinction points are obtained from a photodiode response to plasma brightness. The rise time to final average value is ∼3 s for both. For all temperature measurements, a constant quartz emissivity value of 0.93 was used.

3. Results

3.1. Plasma only

After locating the sensor centreline point of the tube, the aim was to adjust the XYZ and θ positions to achieve an intersection of the optical field with the inner wall that lies between the two electrodes. The sensor starting positions are chosen to ensure the optical edge at the minimum spot size is located as close as possible to the end of the tube inner wall. Three example starting positions are illustrated in figure 6 and Y(0), $Z(0)$ and $\theta(0)$ initial values along with the resultant focal spot diameter, D, is given in table 1. The dashed optic field profile indicates the limit of Z-travel while maintaining $c > 0$. The inner wall temperature profile, figure 7, was obtained for each starting setup in figure 6, by varying the clearance, c, from zero up to the maximum possible, given in table 1. Profile A is dominated by the temperature at the lower electrode region and is constant with c. The profile C diameter at the wall is >4 mm and hence is greater than the plasma area. The temperature increases as the spot moves down since less of the cooler wall above the plasma region is included in the temperature measurement. In profile B, the spot size and location represent the closest match to the plasma region. The temperature decreases as the spot moves away from the powered electrode. The final position is taken therefore from the maximum temperature point of profile B and is given by $Y = 4.91$ mm, $Z = 8.15$ mm, $\theta = 33.75$, $c \sim 0$ mm, with a spot diameter of 2.94 mm.

In a He plasma, the average temperature variation with power, figure 8(a), follows an almost linear relationship with minimal difference between inner and outer wall temperatures while for argon, a sub-linear relation is observed and the outer wall temperature is 2 °C–4 °C higher than the inner. The temperature differences between inner and outer wall are of similar magnitude to error margin of individual readings. Nevertheless, there is evidence that the plasma electrode temperature increases when the plasma is operated with argon. This may cause some external heating of the quartz capillary. With increasing flow, the gas temperature decreases for both gases, figure 9. The introduction of Ar into He changes the plasma impedance and at the lowest flow rate, the gas temperature falls to a minimum when the Ar:He fraction reaches 40:60, figure 10. A plot of net power absorbed against mixture ratio shows the temperature fall is due to a reduction in absorbed power with mixture variation.

We also obtained TC measurements close to the gas outlet. Using an unshielded type K thermocouple resulted in large inaccuracies due to RF interference. To overcome this an earthed shield was incorporated around the TC tip, which was set ∼20 mm from the outlet of a similar plasma configuration which had a greater clearance to accommodate the bulky TC. Measurements required up to 300 s to reach equilibrium and the final measured temperature variation with power at 1 slm flow was from 34 °C to 55 °C. Finally, a number of different insulating probes were placed at the gas outlet and temperature stabilised in the gas flow. One probe consisted of a polymer tube of diameter ∼1 mm covered with black tape while the other was a thin 0.5 mm black insulated wire. The IR sensor, in vertical mode, figure 1(b), was then focussed on these probes

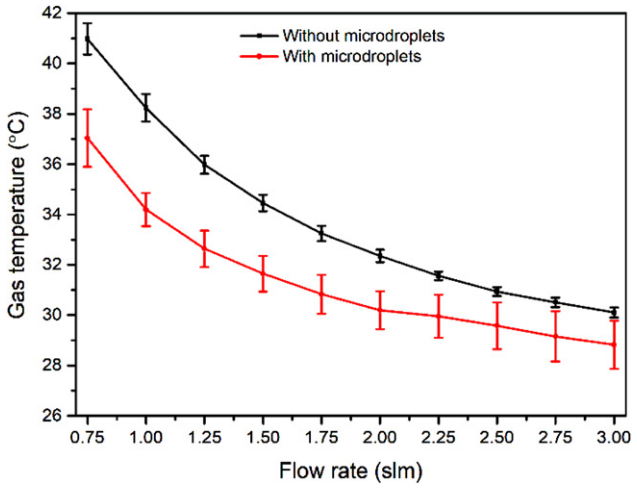

Figure 12. Gas temperature versus total He gas flow rate with and without microdroplets, for a fixed RF power of 0.3 W. Error bars represent the standard error ($n = 3$).

and a temperature reading obtained. An emissivity value of 1 was assumed for both. In He (0.58W, 0.5 slm) the measured temperature was 38 °C and 49 °C for the tube and wire, respectively, while the inner wall temperature at these conditions was 44 °C to 46 °C. In Ar (0.58 W, 0.5 slm) the measured temperature was 36 °C and 39 °C for the tube and wire, respectively, while the inner wall temperature at these conditions was 43 °C to 45 °C.

3.2. Plasma with microdroplets

Inclusion of microdroplets into the plasmas causes a reduction of the gas temperature. For a total He gas flow of 1.5 slm, the absolute temperature decreased by $\geqslant$6 °C at the lowest power and by 12 °C at the highest power, figure 11. The temperature sensitivity to power variation was also reduced. The reduction in temperature with the addition of microdroplets was most noticeable at the lower flow rates, figure 12. At the highest flow (3 slm) the temperature difference was $\sim$1 °C.

4. Discussion

The use of plasma-exposed microdroplets has important potential for delivering plasma-activated liquids and on-demand nanoparticles downstream over rapid timescales. Their chemistry, lifetime and transport however will be sensitive to the gas temperature in the plasma. It is well-known that the addition of small quantities of electronegative gases, e.g. O_2 or H_2O, can increase the gas temperature in noble gas plasmas [2, 42] and hence the possibility exists for accelerated gas heating as the droplet evaporation proceeds. However, under current conditions, the reduction in gas temperature with microdroplet addition indicates that other factors, including evaporative cooling, may be involved. The significance of such cooling depends on droplet number and evaporation rate.

We have previously estimated average droplet evaporation rates by comparing lognormal droplet size and velocity distributions with and without plasma exposure and fitting to a D^2—time profile [6, 39]. For the conditions in this study, the evaporation rate was $\sim 5 \times 10^{-8}$ m^2 s^{-1}. The maximum droplet rate, obtained from the liquid flow rate and the droplet size distribution, is 5×10^4 s^{-1} and the total energy flux (power) required, from the plasma, for this level of evaporation is 18 mW. For the case where droplet and gas travel at same velocity, we used a simplified version of the Abramzon and Sirignano model for droplet vaporisation which indicated that gas heating supplies a maximum energy flux of 3 mW, i.e. over 80% of the evaporation is due to droplet bombardment by charged species [43]. Heinisch *et al* observed experimental evaporation rates in flowing dry N_2, without plasma, approximately one order of magnitude lower than found here, supporting the conclusion that evaporation is dominated by charged particle heating of the droplet [44].

We observed a reduction in gas temperature when droplets are introduced while the power absorbed remains constant. From heat capacity considerations, the maximum difference in temperature (10 °C at 1.5 SLM and 0.3 W) is equivalent to a power difference of 200 mW. At the highest flow, the small reduction in temperature is equivalent to $\sim$40 mW. Therefore across all conditions, the contribution of evaporative cooling (18 mW) is insufficient to account for the full temperature reduction. The introduction of electronegative gases is known to affect power absorption efficiency as the plasma couples less effectively to negative ions. In a separate study, we have observed this effect as H_2O content in the plasma reaches $\sim$3000 ppm. However, with a maximum droplet flow rate of 5×10^4 s^{-1}, the evaporation contributes a maximum of 23 ppm to the average H_2O content in the plasma and hence the impact of enhanced humidity is negligible. Although the evaporated water is more likely to diffuse slowly away from the droplet, $\sim$100 μm over the plasma flight time, rather than disperse uniformly throughout, the vast majority of the plasma volume remains in its original dry and electropositive state.

Plasma ion density variation also impacts on gas temperature through ion—neutral collisions [20, 42, 44]. Figure 8(a) shows an almost linear relationship between gas temperature and power, for He, and we expect plasma density to scale linearly with absorbed power. In figure 8(b), Ar, the relationship is sub-linear. On introducing droplets, any reduction in plasma density while constant power is maintained implies that the loss terms in the power balance equation increase; these include collisional energy lost per electron-ion pair created and the mean kinetic energy lost per electron or ion lost, which depends on T_e. Therefore droplet introduction may lead to a reduction in plasma density and increase in electron temperature, while the absorbed power remains approximately constant.

Successful implementation of droplets in plasma technology for application in areas such as plasma medicine, agriculture and microreaction chemistry requires knowledge and control of gas temperature and evaporation kinetics. Future developments include increasing droplet flow rate while

reducing diameter, gas velocity and extending the plasma flight time. Under current conditions only the smaller droplets (<4 μm) evaporated totally, resulting in a loss of ~5% of the total droplet number and ~0.05% of the total liquid flow volume. For a ten-fold increase in droplet rate and a reduction to an average diameter of 5 μm, while maintaining constant gas flow, the added water content increases to 2000 ppm while the evaporative cooling power also increases to ~700 mW. This provides an indication of the future scope for parameter optimisation.

5. Conclusions

Continuous gas temperature measurement in plasmas is important for many applications, particularly for verifiable monitoring and control of plasmas for medical treatment. We have shown the accurate measurement of gas temperature using a small-spot IR temperature probe focussed on the outer quartz wall. Calibration was obtained via careful measurement of the temperature of the inner wall in direct contact with the plasma, to account for heat loss across the thin quartz tube. For He plasmas, the temperature difference between inner and outer walls was not detectable, within the error margin. For argon, the outer wall was a few degrees hotter. This may be due to additional heating by the external electrodes, since the Ar required greater applied power for the same net power. While the emissivity of quartz is reasonably constant at 0.93, Cu emissivity can vary widely depending on surface condition of the metal. We estimate the electrode temperature between 50 °C and 80 °C. Electrode heating of the quartz outer surface may therefore lead to an overestimation of gas temperature. Plasma gas temperature was observed to increase, as expected, with increasing power and reduced gas flow. The maximum temperature over the full operating range was <50 °C and little difference was observed between pure He and Ar plasmas. For Ar/He mixtures, the fall in temperature on adding Ar is clearly due to the reduction in absorbed power caused by a change in the electrical characteristics of the plasma. The non-invasive low-cost IR probe demonstrated sub-second resolution and performs much better than bulky shielded thermocouple probes that obstruct the gas flow and have a response time of many minutes. Compared to expensive thermal image cameras that can resolve small plasma dimensions, the small-spot IR sensor can be kept *in situ* and its output directly used for feedback control. The sensor also provides useful temperature information for more complex plasma configurations. We observe a cooling of the plasma on introduction of a micro-droplet stream. Previous estimates of such temperatures using OES fitting had a wide error margin (~50 °C) and suggested an average of >75 °C. This is an important parameter in modelling the droplet evaporation rate and the resultant enhancement of overall humidity. The observed fall can be attributed to evaporative cooling and since an increase in humidity generally leads to increased gas heating, these results indicate that the average humidity remains approximately constant and confirms previous droplet measurements which show limited size reduction due to evaporation during transit through the plasma [6].

Acknowledgments

Funding from Engineering and Physical Sciences Research Council (EPSRC EP/R008841/1 and EP/K006088/1) is acknowledged.

ORCID iDs

N Hendawy https://orcid.org/0000-0002-0248-1341
D Mariotti https://orcid.org/0000-0003-1504-4383
P Maguire https://orcid.org/0000-0002-2725-4647

References

[1] Zhou S, Su L, Shi T *et al* 2019 *J. Phys. D: Appl. Phys.* **52** 265202
[2] Bruggeman P J, Sadeghi N, Schram D C and Linss V 2014 *Plasma Sources Sci. Technol.* **23** 023001
[3] Aramaki M, Okumura Y, Goto M, Muto S, Morita S and Sasaki K 2005 *Jpn. J. Appl. Phys.* **44** 6759–63
[4] Fridman A A, Boufendi L, Hbid T, Potapkin B V and Bouchoule A 1996 *J. Appl. Phys.* **79** 1303–14
[5] Schmidt-Bleker A, Reuter S and Weltmann KD 2015 *J. Phys. D: Appl. Phys.* **48** 175202
[6] Maguire P D, Mahony C M O, Kelsey C P *et al* 2015 *Appl. Phys. Lett.* **106** 224101
[7] Yoon S Y, Yi C, Eom S *et al* 2017 *Phys. Plasmas* **24** 075001
[8] Bazavan M, Teodorescu M and Dinescu G 2017 *Plasma Sources Sci. Technol.* **26** 221502
[9] Walsh J L and Kong M G 2007 *Appl. Phys. Lett.* **91** 2005–8
[10] Mariotti D, Shimizu Y, Sasaki T and Koshizaki N 2007 *J. Appl. Phys.* **101** 1–8
[11] Gulec A, Bozduman F and Hala A M 2015 *IEEE Trans. Plasma Sci.* **43** 786–90
[12] Tuszewski M 2006 *J. Appl. Phys.* **100** 0–5 053301
[13] Jayapalan K K and Chin O H 2015 *AIP Conf. Proc.* **1657** 2629–2636
[14] Hu Y, Yang J, Feng C *et al* 2019 *IEEE Trans. Plasma Sci.* **47** 2629–36
[15] Li S Z, Li Z Y, Wu Y and Zhang J 2018 *Phys. Plasmas* **25** 123516
[16] Li X, Yuan N and Jia P 2012 *Adv. Mater. Res.* **383-390** 5907–11
[17] Sláma J 2012 *Acta Polytech.* **52** 61–4
[18] Brehmer F, Welzel S, Van De Sanden M C M and Engeln R 2014 *J. Appl. Phys.* **116** 123303
[19] Lu X P and Laroussi M 2008 *Appl. Phys. Lett.* **92** 2007–9
[20] Hofmann S, Van Gessel A F H, Verreycken T and Bruggeman P 2011 *Plasma Sources Sci. Technol.* **20** 065010
[21] Verreycken T, Van Gessel A F H, Pageau A and Bruggeman P 2011 *Plasma Sources Sci. Technol.* **20** 024002
[22] Oshita T, Kawano H, Takamatsu T, Miyahara H and Okino A 2015 *IEEE Trans. Plasma Sci.* **43** 1987–92
[23] Kawano H, Takamatsu T, Matsumura Y, Miyahara H, Iwasawa A and Okino A 2018 *Biocontrol Sci.* **23** 167–75
[24] Perekrestov R, Kudrna P and Tichý M 2015 *Plasma Sources Sci. Technol.* **24** 035025
[25] Zhang R and Luo G 2018 *Proc. IEEE Int. Conf. on the Properties and Application of Dielectric Materials* (2018-May) pp 305–10
[26] Gerasimov A V, Kirpichnikov A P and Rachevsky L A 2013 *Therm. Sci.* **17** 1251–4
[27] Chen C J and Li S Z 2015 *Plasma Sources Sci. Technol.* **24** 035017

[28] Bruggeman P and Brandenburg R 2013 *J. Phys. D: Appl. Phys.* **46** 464001
[29] Iseni S, Michaud R, Lefaucheux P, Sretenović G B, Schulz-Von Der Gathen V and Dussart R 2019 *Plasma Sources Sci. Technol.* **28** 065003
[30] Knoerzer K, Murphy A B, Fresewinkel M, Sanguansri P and Coventry J 2012 *Innovat. Food Sci. Emerg. Technol.* **15** 23–30
[31] Mazouffre S, Echegut P and Dudeck M 2007 *Plasma Sources Sci. Technol.* **16** 13–22
[32] Fu W, Zhang C, Nie C, Li X and Yan Y 2019 *Appl. Phys. Lett.* **114** 254106
[33] Engelhard C, Scheffer A, Maue T, Hieftje G M and Buscher W 2007 *Spectrochim. Acta Part B At. Spectrosc.* **62** 1161–8
[34] Dowling D P, Donegan M, Cullen P J, Law V J and Milosavljevic V 2014 *IEEE Trans. Plasma Sci.* **42** 2426–7
[35] Jang J, Choe W, Peterson B J *et al* 2018 *Curr. Appl. Phys.* **18** 461–8
[36] Askari S, Levchenko I, Ostrikov K, Maguire P and Mariotti D 2014 *Appl. Phys. Lett.* **104** 163103
[37] Bruggeman P, Iza F, Guns P *et al* 2010 *Plasma Sources Sci. Technol.* **19** 015016
[38] Motret O, Hibert C, Pellerin S and Pouvesle J M 2000 *J. Phys. D: Appl. Phys.* **33** 1493–8
[39] Maguire P, Rutherford D, Macias-Montero M *et al* 2017 *Nano Lett.* **17** 1336–43
[40] Bennet E D, Mahony C M O, Potts H E *et al* 2016 *J. Aerosol Sci.* **100** 53–60
[41] Micro-Epsilon 2020 thermoMETER CT infrared sensor Datasheet https://micro-epsilon.com/temperature-sensors/thermoMETER_CT_basic/?sLang=en
[42] Mariotti D 2008 *Appl. Phys. Lett.* **92** 2006–9
[43] Abramzon B and Sirignano W 1988 *Int. J. Heat Mass Transf.* **32** 1605–18
[44] Heinisch C, Wills J B, Reid J P, Tschudi T and Tropea C 2009 *Phys. Chem. Chem. Phys.* **11** 9720–8